Quantifying the grain boundary segregation strengthening induced by post-ECAP aging in an Al-5Cu alloy

Hailong Jia [a], Ruben Bjørge [b], Lingfei Cao [c], Hui Song [c], Knut Marthinsen [a], Yanjun Li [a,*]

[a] Department of Materials Science and Engineering, Norwegian University of Science and Technology (NTNU), 7491 Trondheim, Norway

[b] SINTEF Materials and Chemistry, 7465 Trondheim, Norway

[c] College of Materials Science and Engineering, Chongqing University, Chongqing 400044, China

*Corresponding author: Yanjun Li. E-mail: yanjun.li@ntnu.no, Tel.: +47 73551206

Abstract

Hardening on annealing (HOA) has been frequently observed in nanostructured metals and alloys. For nanostructured materials obtained by severe plastic deformation (SPD), HOA has been attributed to the reduction of dislocation sources within grains and grain boundary relaxation during annealing. In the present work, it is shown that when a bimodal grain structured (a mixture of micron-sized and ultrafine grains) Al-5Cu alloy prepared by equal channel angular pressing (ECAP) was subjected to a post-ECAP natural and artificial aging treatments, the alloy shows a completely different precipitation behaviour with an accelerated precipitation kinetics. No coherent θ" or semi-coherent θ' precipitates form in the bulk of grains, while a large fraction of stable incoherent θ precipitates form along high angle boundaries. After artificial aging at low temperatures for a short time, a significant improvement of both ultimate tensile strength and uniform elongation was achieved without sacrificing the yield strength. A systematic microstructure characterization by EBSD, TEM and APT has been carried out to investigate the evolution of grain size, dislocation density and solid solution level of Cu as well as the precipitation of Al-Cu precipitates during natural and artificial aging treatments. A quantitative evaluation of different supposed strengthening mechanisms revealed that the segregation of Cu elements at grain boundaries plays a more important role than grain boundary relaxation and the dislocation source-limited strengthening to compensate the yield strength reduction caused by the decrease in dislocation density and solute content of Cu in solid solution.

Keywords: Aluminum alloy; Aging; Segregation; Precipitation; Tensile properties

1. Introduction

Severe plastic deformation (SPD) techniques, for instance, equal channel angular pressing (ECAP) [1-4], high pressure torsion (HPT) [5-7] and accumulative roll bonding (ARB) [8-10] have been widely applied to produce nanostructured metals and alloys. Here, nanostructured materials refer to materials comprising ultrafine grains (< 1 μm) and/or nano-sized grains (< 100 nm) [8]. The strength of nanostructured Al alloys prepared by SPD is superior to their coarse grained counterparts, which is mainly attributed to grain boundary (GB) strengthening and dislocation strengthening. In sharp contrast to the softening of coarse grained as-deformed materials subjected to annealing, an increase in yield strength accompanied by a reduction of ductility could be achieved in nanostructured metals by a short time annealing at low temperatures without recrystallization or significant grain growth, which is the so-called "hardening on annealing (HOA) phenomenon [11]. Such a phenomenon has been found both in commercial purity (99.2 wt.%) Al [9, 11] and high purity (99.99 wt.%) Al produced by ARB [10, 12]. The HOA effect of the severely deformed metals was attributed to the reduction of the number of dislocation sources caused by the sinking of dislocations at closely spaced high angle boundaries (HABs).

Similar HOA effect has also been observed earlier in nanostructured commercial purity Ti [13], Al-1.5 wt.% Mg [14] and Ni_3Al [15] alloys processed by HPT, which was attributed to defect ordering at or near GBs [13-15]. Actually, defect ordering at or near GBs is in accordance with GB relaxation. The GB relaxation has been proved by high resolution TEM studies [13-15] and differential scanning calorimetry (DSC) measurements [16, 17]. By using DSC, Detor and Schuh [16] found that the heat release scales directly with the GB area, indicating that such an exothermic peak is associated with a GB relaxation process. Valiev et al. [14, 15] suggested that the GB transparency can influence the strength of materials and non-equilibrium boundaries are more transparent, where the GB transparency is defined as a critical value of the applied stress for allowing slip to propagate through a given GB. During annealing, the relaxation of non-equilibrium boundaries happens, where the stored energy in the form of disorder or excess GB defects is released [16, 18] and emission of dislocations from such relaxed GBs becomes difficult [19, 20].

In fact, the HOA phenomenon is observed not only in the metals and alloys processed by SPD, but also in alloys deformed by traditional cold rolling. For example, after annealing at 225 ˚C for 10 min, the AA3103 alloy strip rolled to a strain of ~4.2 showed an increase in ultimate tensile strength (UTS) [21]. It was also found that the magnitude of the gained strength by HOA increased with deformation strains. The exact mechanism causing HOA was not identified, but it was suggested that atom clustering of solute elements may have played a role [21].

The HOA phenomenon has also been observed and extensively studied in dislocation-free nanocrystalline metals and alloys. For example, Ni [22], Ni-W [16, 23] and Ni-Mo [17] alloys prepared by the electrodeposition method. Different from the nanostructured materials produced by SPD, the HOA phenomenon in electrodeposited dislocation-free nanocrystalline materials has been attributed to GB stabilization through GB relaxation [16, 17] and/or GB segregation of alloying elements [17], which leads to the deformation mechanism change from GB-mediated processes [24-27] to generation of extended partial dislocations from GBs [17, 28]. Nowadays, GB segregation has been applied as an effective strategy to stabilize the grain structure of nanocrystalline materials by lowering the GB energy [29-33].

In the present work, the aim has been to further explore the strengthening mechanisms of the HOA phenomenon in SPD processed alloys, and thus post-ECAP aging treatments at low temperatures have been conducted on a bimodal structured Al-5wt.% Cu alloy [34] produced by room temperature ECAP. Systematic investigations on the evolution of grain size, dislocation density, solid solution level of Cu and precipitation of Al-Cu precipitates during post-ECAP aging have been done. It is shown that GB segregation has a strong strengthening effect to the SPD processed alloys in addition to the GB relaxation and dislocation source-limited strengthening.

2. Experimental

The binary Al-5wt.% Cu alloy used in this study was prepared by melting the commercial purity Al and Cu. Prior to ECAP, solution heat treatment was conducted on the Al-5Cu bars with dimensions of 100 mm × 19.5 mm × 19.5 mm, using a salt bath furnace at 500 ˚C for 3 h and then at 540 ˚C for 24 h followed by water quenching. Then, these bars were processed by ECAP through a 90˚ die at RT.

Route A was employed, which means that samples were pressed without rotation between each pass, leading to an imposed equivalent strain of ~1.0 per pass [1]. To lower the friction during pressing, samples were coated with a thin layer of graphite lubricant. The ECAP samples were processed up to four passes, which were labelled as 4P. The as-deformed (4P) samples were stored at RT for half an hour, and then artificially aged in an oil bath at 120 ˚C, 150 ˚C and 185 ˚C for different times.

Samples for microstructural characterization, hardness and tensile test measurements were cut from uniformly deformed regions of the ECAP processed bars, as shown in Fig. 1. Microstructure and composition analyses were carried out by means of electron backscatter diffraction (EBSD), transmission electron microscopy (TEM), scanning precession electron diffraction (SPED) and atom probe tomography (APT). EBSD analyses were conducted on the longitudinal (ND-ED) cross section of the samples. Prior to the EBSD examination, the sample surfaces were electro-polished and ion-milled (Hitachi IM-3000 Flat Milling System) at 3.5 V for 45 min. EBSD was conducted in a Hitachi SU-6600 field emission gun-scanning electron microscope (FEG-SEM) equipped with a Nordif EBSD detector. Thin foils for transmission electron microscopy (TEM) were prepared by twin-jet electro-polishing using a solution of 33% nitric acid in methanol at -30 ˚C. TEM imaging was carried out using the JEOL 2010 TEM and SPED mapping was performed using the JEOL 2010F equipped with the NanoMegas ASTAR system. Needle-shaped samples for atom probe tomography (APT) were prepared by a standard two-stage electro-polishing technique [35]. APT was performed in a CAMECA LEAP 4000 HR type local electrode atom probe at a temperature of 50 K with a pulse fraction of 15%, a pulse rate of 200 kHz and a detector efficiency of 36%. Reconstruction and quantitative analysis of the APT data were performed using the IVAS^{TM} 3.6.12 software.

Mechanical properties were characterized by both hardness and tensile tests. Vickers hardness measurements were performed using a DVK-1S Vickers hardness testing machine under a load of 5 kg, applied for 15 s. The hardness values obtained were averaged from at least six separate measurements. Tensile specimens (with a gauge length of ~5 mm, width of ~4 mm and thickness of ~2 mm) were machined from the bars in the longitudinal direction (Fig. 1). Tensile tests were conducted at RT under a strain rate of 5×10^{-4} s^{-1}, using a MTS 810 hydraulic universal testing machine with a 100 kN capacity.

3. Results

3.1. Microstructure of the as-deformed sample

A typical EBSD orientation image of the as-deformed (4P) sample is shown in Fig. 2. The alloy shows a bimodal grain structure, i.e., in addition to ultrafine grains (< 1 μm), elongated micron-sized grains are also present in the material (Fig. 2(a)). To gain a better insight into the deformation structure of the micron-sized grains, misorientation profiles along and perpendicular to the longitudinal direction of elongated grains were measured. Here, micron-sized grains are categorized into two types: coarse micron-sized grains (larger than 2 μm in any direction) and fine micron-sized grains (~1-2 μm). Fig. 2(b) shows the misorientation profiles along lines L1 and L2 inside a coarse micron-sized grain containing few LABs. Long-range misorientation gradients exist in both directions that are parallel with and perpendicular to the elongated direction. The geometrically necessary dislocation (GND) density can roughly be estimated by the misorientation gradient according to the equation $\rho_{dis} \approx {}^{\theta}/_{b\delta}$ [36], where θ is the accumulated misorientation angle in radians within a distance δ, and b is the Burgers vector. The dislocation density of each coarse micron-sized grain is averaged from directions parallel with and perpendicular to the elongation direction. Based on calculation of five different coarse micron-sized grains, the average GND density is estimated to be ~2.2×10^{14} m^{-2}. In the fine micron-sized grains (e.g., lines L3 and L4 in Fig. 2(a)), long-range misorientation gradients also exist (Fig. 2(c)). The GND density is estimated to be ~1.8×10^{14} m^{-2}, which is slightly lower than that in the coarse micron-sized grains.

3.2. Natural aging behavior of the as-deformed alloy

3.2.1. Hardness

The Vickers hardness evolution of the as-solutionized and the as-deformed (4P) Al-5Cu alloys during natural aging are presented in Fig. 3. As expected, the as-solutionized sample shows a typical natural aging behavior. The hardness rises gradually with increasing time during the early stage of RT-storage, i.e., from ~80 HV to ~115 HV after 16 days. Thereafter, it continues to increase with time but at a much lower rate, reaching a value of ~122 HV after 121 days. This value is higher than that of

the Al-4 wt.% Cu alloy with the same natural aging time investigated in Ref. [37], owing to the higher Cu content in the present study. After 420 days, the hardness is almost the same as that after 121 days.

In comparison, the as-deformed (4P) sample shows a very high initial hardness value which is about twice as that of the as-solutionized sample. With increasing the RT-storage time, the hardness of the as-deformed (4P) sample increases. A peak hardness of ~168 HV is reached after one month, and thereafter it decreases with further increasing the natural aging time. After ~115 days, the hardness value reduces to the initial hardness value of the as-deformed (4P) sample. It can be seen that after storage at RT for more than one year, the hardness is ~7 HV lower than that of the as-deformed (4P) sample.

The electrical conductivity (EC) of the as-deformed (4P) and naturally aged 4P samples was also measured. It is ~21.5 MS/m for the as-solutionized sample and after more than one year RT-storage, it increases to ~22.1 MS/m. For the as-deformed (4P) sample, the electrical conductivity is ~20.5 MS/m, and after RT-storage for more than one year, it increases to ~21.7 MS/m. The increase in electrical conductivity implies that Al-Cu precipitates have formed during natural aging.

3.2.2. Microstructure of the naturally aged alloy

Bright field TEM images and corresponding selected area diffraction pattern (SAD) of the as-deformed (4P) sample with one-month natural aging are shown in Fig. 4. A large fraction of elongated submicron-sized grains with a high dislocation density can be observed. The non-equilibrium GBs are poorly defined and show a curved and diffuse character, indicating a high level of internal lattice stresses and high dislocation densities. The structure of the as-deformed (4P) sample after one-month natural aging (Fig.4 (b)) is similar to that of the as-deformed (4P) sample, which indicates that no significant recovery has happened.

STEM-EDS and TEM-SPED mapping were performed on the as-deformed (4P) sample after one-month natural aging and the corresponding results are shown in Fig. 5. From the STEM image (Fig. 5(a)), it can be seen that a large number of nano-sized precipitates have formed along (sub)grain boundaries. Based on the EDS map (Fig. 5(b)) and diffraction patterns, these precipitates are determined as metastable θ' and equilibrium θ phases. To study the correlation between the precipitates and misorientations of (sub)grain boundaries, a region with less precipitates was analyzed

by SPED and the results are shown in Fig. 5 (c) and (d). As can be seen, most boundaries are LABs, while the precipitates are only observed along HABs. It implies that the θ' and θ phases preferentially precipitate along HABs, which is in agreement with the previous study in Ref. [37]. Usually, the GB precipitates in Al-Cu alloys are the equilibrium θ phase [38]. However, in this study θ' precipitates are also observed (e.g., Fig. 5(d)), most of which distribute along segments of coincident site lattice (CSL) boundaries. This indicates that these special low energy boundaries may favor the formation of θ' phase. It is well known that in solutionized Al-Cu alloys stable θ precipitates can only form after over-aging at relatively higher temperatures [39]. Compared with the as-solutionized sample, after one-month natural aging, the formation of θ precipitates in the as-deformed (4P) samples indicates that the precipitation kinetics is much accelerated.

3.3. Artificial aging behavior of the as-deformed alloy

3.3.1. Hardness and electrical conductivity

The evolution of Vickers hardness of the as-solutionized and the as-deformed (4P) Al-5Cu alloys during artificial aging at three different temperatures is plotted in Fig. 6(a) and (b), respectively. As can be seen from Fig. 6(a), the as-solutionized alloy shows the peak hardness at 40 h and 10 h when aged at 150 ˚C and 185 ˚C, respectively. When aged at a lower temperature, i.e., 120 ˚C, the hardness keeps rising even after 200 h. As illustrated in Fig. 6(b), the as-deformed (4P) samples show a very different age hardening behavior, i.e., a rapid increase in hardness with increasing aging times. The peak aging times are ~2 min, ~1 min and ~40 s for aging at 120 ˚C, 150 ˚C, and 185 ˚C, respectively. After the peak hardness, the hardness decreases with increasing ageing times and the decreasing rate is slower during aging at 120 ˚C than that at 150 ˚C and 185 ˚C.

The electrical conductivity of the as-deformed (4P) samples during artificial aging are shown in Fig. 6(c) and Table 1. It can be seen that the electrical conductivity increases with increasing aging times. When aging at 150 ˚C, the rate of increase is much faster than that of aging at 120 ˚C. The monotonic increase in electrical conductivity indicates a decrease in solid solution level of Cu in the matrix due to precipitation of precipitates, which is faster when aging at higher temperatures.

3.3.2. Tensile properties

Based on the hardness evolution shown above, different aging heat treatments were selected to study the influence of artificial aging on mechanical properties. The engineering tensile stress-strain and true stress-strain curves of the as-deformed (4P) and aged samples are shown in Fig. 7. Table 1 summarizes the tensile property values, i.e. yield strength (YS), ultimate tensile strength (UTS), uniform elongation (UE) and elongation to failure (EF). Interestingly, after aging at 120 ˚C for 2 min, both the UTS and UE are significantly improved (~14 MPa and ~0.9% for the UTS and UE, respectively) while the YS keeps almost the same as that of the as-deformed (4P) sample. However, aging for longer times or at higher temperatures causes a significant reduction of both YS and UTS, but increase in UE. For example, after aging at 120 ˚C for 15 min, the UE is improved from 5.1% to 8.7% at a cost of a significant YS reduction (~ 53 MPa). However, after aging at 120 ˚C for 30 min, no further improvement of UE can be observed. After aging at 150 ˚C, there is an increase in UE, while the YS and UTS are decreased rapidly with increasing aging times.

3.3.3. Microstructure of the artificially aged alloy

Fig. 8(a)-(c) shows the EBSD orientation maps of the as-deformed (4P) samples after aging at 120 ˚C and 150 ˚C. As compared to the as-deformed (4P) sample (Fig. 2(a)), no significant change of the grain structures can be observed after aging at 120 ˚C for 2 min and 30 min (Fig. 8(a) and (b)). As shown by the misorientation profiles of lines L1-L6, long-range misorientation gradients still exist in both coarse and fine micron-sized grains. For the 120 ˚C-2 min sample, the GND densities estimated from misorientation gradients are ~2.0×10^{14} m^{-2} and ~1.5×10^{14} m^{-2} for coarse and fine micron-sized grains, respectively, which are about the same as that of the as-deformed (4P) sample. With further increasing the aging time to 30 min, the GND densities are estimated to be ~1.8×10^{14} m^{-2} and ~1.3×10^{14} m^{-2} for coarse and fine micron-sized grains, respectively, showing a slight reduction in dislocation density.

After aging at 150 ˚C for 96 h (Fig. 8(c)), a big change in grain structure has happened. A large density of LABs with misorientations 6-14˚ are formed within the coarse micron-sized grains. For the coarse micron-sized grains, as shown by the misorientation profiles, long-range misorientation gradients still exist along the lines L7 and L8. However, the misorientation gradients are lower than

that of the two previous heat treatments. The GND dislocation densities are estimated to be ~1.5 × 10^{14} m^{-2} in the coarse micron-sized grains. There is nearly no misorientation gradients inside the fine micron-sized grain (the line L9 in Fig. 8(c)), which means that recovery has happened. It can be seen that the dislocation density in the fine micron-sized grains decreases more rapidly than that in the coarse micron-sized grains during artificial aging.

Fig. 9 shows STEM images of the as-deformed (4P) samples after aging at 120 ˚C for 2 min and 30 min. After aging at 120 ˚C for 2 min, a large numbers of nano-sized precipitates are formed along GBs, while no precipitates can be observed in grain interiors. This is completely different from the typical precipitation behavior of the undeformed specimens during artificial aging. A closer examination shows that a large fraction of the precipitates are with a plate-shape and distribute along HABs, like continuous thin films. Meanwhile, some nano-sized globular shaped precipitates could also be observed. Fig. 9(c) and (d) show precipitates in the 120 ˚C-30 min sample. Compared to the 120 ˚C-2 min sample, the density of precipitates is much higher, and meanwhile, most of the precipitates show a coarser and more globular morphology, which suggests that coarsening/ripening of precipitates has occurred. The precipitation of a higher fraction of precipitates is consistent with the electrical conductivity evolution (Fig. 6(c)).

After aging at 120 ˚C for 2 min, a strong segregation of Cu at GBs has also been observed, especially in those HABs without precipitates. Fig. 10 shows two examples, where the concentration profiles of Cu across a GB measured by EDS line scanning are included. The measured Cu concentration at the GB is about 2 times as that of the surrounding matrix, showing a strong GB segregation.

TEM-SPED mapping was also conducted on the 120 ˚C-2 min and 120 ˚C-30 min samples. As can be seen from Fig. 11(a)-(c), all the precipitates are located at HABs. The majority of the precipitates have been identified as the θ phase, while θ' precipitates can occasionally be observed. The block shape of the θ' phase is different from the morphology of normal thin plate-shaped θ' precipitates. The globular shaped θ precipitates are mainly locating at triple junctions of GBs. Misorientations along the lines L1-L4 within two types of grains were measured, i.e., nano-sized grains (< 100 nm) and submicron-sized grains (100 nm-1 μm). From Fig. 11(d) and (e), it can be seen

that within the submicron-sized grains (e.g., L1 and L3), most of the point-to-point misorientations are lower than 1.5˚. However, the large long-range misorientation gradients can still be detected. The GND densities are estimated to be ~1.2×10^{15} m^{-2} and ~8.0×10^{14} m^{-2} for the 120 ˚C-2 min and 120 ˚C-30 min samples, respectively. However, there is no long-range misorientation gradient inside nano-sized grains (e.g., L2 and L4), indicating a rather low density of GNDs. In fact, the long-range misorientation gradient within nano-sized grains of the as-deformed (4P) sample is already low, where nearly complete dynamic recovery has occurred during the ECAP deformation.

To further examine if there is any atom clusters or GP zones forming in the bulk of grains, APT analyses were conducted on the 120˚C-2 min sample. Fig. 12 (a) shows the 3D distribution of Al and Cu atoms in a representative sample tip containing a GB segment. An enrichment of Cu at GB and a Cu-depleted region around the GB can be observed. Fig. 12(b) shows that the Cu-rich region at the GB is an Al-Cu precipitate, which has grown along the curved GB. The highlighted small region across the precipitate in Fig. 12(b) is enlarged and shown in Fig. 12(c), where the depletion of Cu near the GB can be quite clearly seen. As shown by the 1D concentration profile across the GB (Fig. 12(d)), the atomic fraction of Cu within the precipitate fluctuates in the range of ~25-35%, which is close to that of the θ-Al_2Cu phase.

Analysis of the data shows that no Cu atom clusters larger than 10 atoms (distance between each atom $\leq$ 0.7 nm) could be detected. Thus, the atom cluster strengthening mechanism would not be expected in the present study. Even if there are few Cu atom clusters, their effect would be insignificant, because it has been suggested that the Cu-Cu clusters have a negligible impact on the age hardening behavior [40, 41].

Due to the segregation of Cu and formation of precipitates along GBs, the solid solution strengthening in the aged samples is supposed to decrease. However, as observed from the tensile tests, the YS of the 120˚C-2 min sample is nearly the same as the as-deformed (4P) sample, which implies that additional strengthening mechanisms may have contributed to the YS. In comparison to the as-deformed (4P) sample, the GND density in grains with sizes larger than 100 nm (fraction > 99.5%) exhibits a negligible reduction. It indicates that the dislocation source-limited strengthening

mechanism is rather limited. Therefore, the question is what strengthening mechanisms have compensated the strength reduction caused by the decreased solid solution strengthening.

4. Discussion

4.1. Accelerated aging behavior

In comparison to the as-solutionized alloy, the as-deformed (4P) sample shows a completely different aging behavior during both natural and artificial aging. Firstly, precipitation is very fast. For instance, after only 2 min when aging at 120 ˚C, a large amount of θ' and θ particles have formed, while no GP zones and metastable θ" precipitates can be observed. This is the same for the as-deformed (4P) samples after one-month storage at RT. Secondly, precipitation only occurs along HABs, while no precipitates could be observed on LABs or within the bulk of grains.

The accelerated precipitation can be attributed to the local environment of the deformation microstructure, in terms of the formation of a large fraction of non-equilibrium HABs (~58%). The non-equilibrium HABs are more disordered and expected to accommodate more solute elements than fully relaxed boundaries [42] and LABs. During deformation, forced migration of GBs may result in a strong segregation of Cu from the swept matrix. At the same time, the high vacancy concentration and dislocation density can accelerate the diffusion of Cu atoms from the bulk to GBs. As a result, the HABs are over-supersaturated with Cu solutes. Thus, there is a large local driving force for the precipitation of Al-Cu precipitates at the HABs, which could even happen during natural aging. However, due to the disordered structures at HABs, it is difficult to form ordered GP zones and coherent θ" precipitates, while incoherent θ precipitates can form directly during natural and artificial aging.

4.2. Strength and ductility improvement by post-ECAP aging

The strength and ductility of polycrystalline materials are usually considered mutually exclusive. However, an unexpected striking stress-strain response can be observed after aging at 120 ˚C for 2 min. The YS is almost the same as the as-deformed (4P) sample, while both the UTS and UE are improved. For the as-deformed (4P) sample, the YS (σ_y) can be described in terms of three

strengthening mechanisms, including GB strengthening (σ_{GB}), dislocation strengthening (σ_D) and solid solution strengthening (σ_{SS}):

$$\sigma_y = \sigma_0 + \sigma_{GB} + \sigma_D + \sigma_{SS} \quad \text{Eq. (1)}$$

where σ_0 is the lattice friction stress in pure Al.

For polycrystalline metals, the influence of grain size on the YS can be described by the classical Hall-Petch (HP) relationship as given in Eq. (2), where d is the average grain size and k is a material-dependent constant.

$$\sigma_y = \sigma_0 + kd^{-1/2} \quad \text{Eq. (2)}$$

As shown in Fig. 8, after aging at 120 ˚C for 2 min and 30 min, no significant grain structure change can be observed. Thus, GB strengthening is thought to be unchanged, given that the k value is a constant.

Dislocation strengthening (σ_D) is dependent on the dislocation density of materials. The GND density obtained based on the EBSD results is summarized in Table 2. It is difficult to calculate the GND density inside the nano-sized (< 100 nm) grains (in both the as-deformed and aged 4P samples), because the long-range misorientation gradients are very low within these grains and therefore the GND density can be neglected. Overall, as can be seen from Table 2, after aging at 120 ˚C for 2 min, there is almost no change in the GND density within the grains with sizes > 100 nm. Even when aged at 120 ˚C for 30 min, there is a limited reduction of the GND density in all the measured grains.

According to classical work hardening theories, the strength contribution from dislocation strengthening is given by the following relationship [43]:

$$\sigma_D = M\alpha Gb\sqrt{\rho_{dis}} \quad \text{Eq. (3)}$$

where α is a numerical constant measuring the efficiency of dislocation strengthening, G is the shear modulus, and b is the Burgers vector. The values of these parameters are taken as: M = 3, α = 0.3, G = 27 GPa and b = 2.86×10^{-10} m [36]. The decreased dislocation strengthening caused by the reduction of dislocation density has been calculated and quantitatively listed in Table 3. Note that the results are based on the dislocation density evolution estimated by EBSD and thus, statistically stored dislocations (SSDs) are not included. The fraction of submicron-sized grains (ultrafine grains) and

micron-sized grains is measured to be ~70% and 30%, respectively. Thus, the overall decreased dislocation strengthening ($\Delta\sigma_D$) is estimated to be ~9 MPa and ~41 MPa for the 120 ˚C-2 min and 120 ˚C-30 min samples, respectively.

According to Matthiessen' rule [44], the electrical resistivity (ρ) of an alloy at a given temperature (T) is normally written as [45-47]:

$$\rho = \rho_0 + \rho_{SS} + \rho_D + \rho_{GB} + \rho_V + \rho_P \quad \text{Eq. (4)}$$

where ρ_0 is the resistivity of single crystalline pure Al with no lattice defects, ρ_{SS}, ρ_D, ρ_{GB}, ρ_V, and ρ_P are the resistivity due solute atoms, dislocations, GBs, vacancies and particles, respectively. Thus, an increase in the total electrical resistivity can be expressed as:

$$\Delta\rho = \Delta\rho_{SS} + \Delta\rho_D + \Delta\rho_{GB} + \Delta\rho_V + \Delta\rho_P \quad \text{Eq. (5)}$$

which can be further expressed as:

$$\Delta\rho = \Delta\rho_{SS} + A\Delta L_D + B\Delta S_{GB} + C\Delta N_V + \Delta\rho_P \quad \text{Eq. (6)}$$

ΔL_D, ΔS_{GB}, and ΔN_V are the change in dislocation density, GB density and vacancy concentration, respectively. A, B and C are the contributions of unit dislocation density, GB density and vacancy concentration to the resistivity, respectively. A, B and C are constants, taken as 2.7×10^{-25} Ωm^3 [48], 2.6×10^{-16} Ωm^2 [48] and $(26 \pm 5) \times 10^{-9}$ Ωm/at.% [49], respectively.

After aging at 120 ˚C for 2 min, compared to the as-deformed (4P) sample, the change in electrical resistivity is ~3×10^{-9} Ωm. It is estimated that the reduction in dislocation density is in the order of 10^{-14} m^{-2}. Thus the reduction in electrical resistivity due to the dislocation density change ($A\Delta L_D$) is ~2.7×10^{-11} Ωm, which is negligible compared with the total decrease in electrical resistivity. Since the grain size of the 120˚C-2 min sample is unchanged, the change in electrical resistivity due to the change of GB density can be ignored. Besides, it has been suggested that the influence of vacancy defects on electrical resistivity is negligible [45, 47, 50-52]. The vacancy concentration has been estimated to be ~10^{-4} [53] immediately after SPD compared to an equilibrium concentration of ~10^{-10} [37]. The upper limit of the change in vacancy concentration by aging at 120 ˚C for 2 min is ~10^{-4}. Therefore, the reduction of the electrical resistivity $\Delta\rho_V$ is ~2.6×10^{-12} Ωm, which can be neglected as well. In addition, it is well known that the contribution of particles to the

electrical resistivity is much less than that of the same amount of particle forming elements in solid solution.

Thus, the electrical resistivity is dominated by the change of the concentration of solute elements. The electrical conductivity ($EC = \frac{1}{\rho}$) change can be used to evaluate the change of solid solution level of Cu. As expressed in Eq. (4) [54],

$$\Delta\rho = \Delta\frac{1}{EC} = 0.0032\ \Delta Cu_{ss}\% \qquad \text{Eq. (7)}$$

the unit of EC is MS/m and Cu_{ss}% is the weight percentage of Cu in solid solution, respectively. After aging at 120 ˚C for 2 min and 30 min, the electrical conductivity increases from 20.5 to 21.6 and 22.7 MS/m, respectively. By using Eq. (7), the reduction of the solid solution level of Cu can be estimated to be ~0.78 wt.% and ~1.48 wt.% after aging at 120 ˚C for 2 min and 30 min, respectively. Thus, the decreased solid solution strengthening ($\Delta\sigma_{SS}$) is estimated to be ~26 MPa and ~49 MPa for the 120 ˚C-2 min and 120 ˚C-30 min samples, respectively, given that solid solution strengthening caused by per weight percent of Cu is ~33 MPa [55]. However, as can be seen from Table 1, the YS of the 4P+120 ˚C-2 min sample is nearly unchanged compared to the as-deformed (4P) sample, which indicates that the decreased dislocation strengthening (~9 MPa) and solid solution strengthening (~26 MPa) have been compensated by some additional strengthening mechanisms.

It is well known that Al-Cu alloys are age-hardenable by aging treatment due to the formation of high density of nano-sized θ" and θ' precipitates within grains and that the incoherent θ phase formed during over-aging has a very limited strengthening effect. However, by carefully examining the 120 ˚C-2 min sample using STEM, SPED and APT, no indication of age hardening precipitates or even obvious Cu atom clusters were observed within grains. Therefore, for the 120 ˚C-2 min sample, the precipitation strengthening and cluster strengthening are not expected.

Dislocation source-limited hardening has been proposed to be an important strengthening mechanism in nanostructured metals [10, 11, 56, 57]. During annealing, dislocations inside ultrafine and nano-sized grains that can easily glide are annealed out, resulting in a higher YS required to activate new dislocation sources during tensile testing. Based on the EBSD results, after aging at 120˚C for 2 min, the decrease in dislocation density within both micron-sized grains and submicron-

sized grains is negligible. It means that the dislocation source-limited hardening mechanism seems not significant for the micron-sized grains and submicron-sized grains in the present study. For the nano-sized grains, it is difficult to quantitatively evaluate the dislocation density evolution since the long-range misorientation gradients are already very low in the as-deformed (4P) sample. However, the area fraction of the nano-sized grains in the as-deformed (4P) sample is only ~0.5%, so the contribution from the dislocation source-limited hardening to the strength increase is rather limited if there is any.

Another possible strengthening mechanism is the relaxation of non-equilibrium boundaries caused by annealing. The rationale of strengthening caused by GB relaxation is that it is more difficult for such relaxed GBs to emit dislocations, thus making the material more resistant to yielding under applied stresses [16, 58]. In comparison to the reported annealing temperatures and times in terms of the HOA phenomenon in SPD processed Al metals or alloys, the present aging (annealing) temperature and time are significantly lower and shorter, e.g., 120 ˚C-2 min vs. 150 ˚C-30 min [11] and 175 ˚C-30 min [10]. Therefore, the GB relaxation is rather limited. This can also be demonstrated by TEM images, where no obvious difference of GB structures between the as-deformed (4P) (Fig. 4(b)) and 4P+120˚C-2 min sample (similar to the TEM images in Fig. 4(b)) can be observed. In Ref. [10], the as-deformed high purity (99.99 wt.%) Al is with an average grain size of ~0.7 μm, similar to that of the present study. After annealing at 175 ˚C for 30 min, the increase in YS is ~6.7 MPa in comparison with the as-deformed sample. By considering the dislocation strengthening and GB strengthening (misorientations > 3˚), the difference between the experimental and calculated YS was estimated to be ~10 MPa, which was thought to be caused by the dislocation source-limited mechanism. If the GB relaxation strengthening is considered, it is less than 10 MPa. It indicates that in the present study, GB relaxation strengthening (< 10 MPa) is not the main strengthening mechanism that compensates the reduced YS (~35 MPa) caused by decreased dislocation strengthening and solid solution strengthening.

For SPD processed UFG materials, it has been suggested that deformation induced segregation of solute atoms along GBs may hinder the emission of dislocations from GBs, improving the strength of materials [59]. For example, an UFG 1570 Al alloy (containing 5.7 wt.% Mg) produced by HPT,

was found to exhibit a very high strength, considerably exceeding the Hall-Petch predictions for ultrafine grains [59]. Segregation of Mg along GBs in the as-deformed samples has been verified by APT [59], which was supposed to be the reason for the high strength. In the present work, a post-ECAP aging will further enhance the GB segregation.

After aging at 120 ˚C for 2 min, the local enrichment of Cu at GBs has been confirmed by the EDS line profile analysis (Fig. 10). During deformation, GBs can act as barriers to dislocation slip causing a pile-up of dislocations in front of GBs. Only when the stress concentration is larger than a certain critical value, dislocation slip in a neighboring grain can be initiated and then the glide can continue. The supersaturation of Cu solute at GBs can contribute to the YS increase by modifying the GB characteristic. The k value in the Hall-Petch equation (Eq. (2)) is defined as [60]:

$$k = M\sqrt{\tau_c 4Gb/((1 - \nu)\pi)} \qquad \text{Eq. (8)}$$

where M is the Taylor factor, τ_c is the critical stress for slip to break through GBs, G is the shear modulus, and ν the Poisson's ratio. The segregated Cu atoms can effectively increase the k value in Eq. (8) by increasing the critical stress τ_c. Recently, segregation of Cu and its effects on the strength of a symmetrical tilt GB in Al has been investigated by the first-principles calculation [61, 62]. It shows that Cu segregation leads to a significant decrease in the GB energy and induces a cohesion enhancing effect on GBs in Al alloys. MD simulations [63] also show that GB energy decreases as solute concentration at GBs increases while the YS scales inversely with GB energy, indicating that solute segregation should lead to a significant strengthening effect.

A further examination of the results in Refs. [10, 11] has been performed. After annealing at 150 ˚C for 30 min, the YS is increased by ~22 MPa [11] and ~5.2 MPa [10] for the 99.2 wt.% and 99.99 wt.% impurity Al alloys, respectively. It implies that the HOA effect becomes more pronounced in the nanostructured Al samples with higher impurity concentrations. With higher impurity content, there will be much more solute atoms segregated to GBs during annealing, increasing the slope (k value) of the Hall-Petch relationship and thus increase the YS. In addition, as clarified by TEM (Fig. 9(b)), some of the segregated Cu atoms along HABs have transformed into very thin and continuous plate-shaped precipitates, which are quite different from the conventional morphology of particles along

HABs. Here, we speculate that the high coverage of HABs by the very thin and continuous plate-shaped precipitates may also play the same role as the supersaturation of Cu solute at GBs, contributing to the YS increase.

A schematic drawing to show the evolution of solute segregation and precipitation is shown in Fig. 13. After aging at 120 ˚C for 2 min, the loss of strength caused by the decreased dislocation strengthening and solid solution strengthening can be compensated by the strength increase due to segregation of Cu atoms at GBs and GB relaxation, probably as well as the continuous thin plate-shaped precipitates along GBs. With further increasing the aging time, more Cu solutes diffuse to GBs. In this case, the solid solution level of Cu will further decrease, as evidenced by the electrical conductivity increase. At the same time, the coarsening will develop the GB precipitates into a coarse globular shape, which are less continuous. This can also result in depletion of Cu close to the precipitates along GBs and thus reduces GB segregation strengthening. Moreover, compared to the continuous thin plate-shaped precipitates, the less continuous and coarse globular precipitates make GBs less covered. In this case, the strength increase due to GB relaxation, segregation of Cu atoms and continuous thin plate-shaped precipitates along GBs cannot compensate the reduced dislocation strengthening and solid solution strengthening, making the YS decrease.

It is interesting to see that both the UTS and UE are improved after aging at 120 ˚C for 2 min. An analysis on the work hardening rates of the as-deformed (4P) and the 120 ˚C-2 min samples has been done. As can be seen from Fig. 14, the work hardening rate of the 120 ˚C-2 min sample is higher than that of the as-deformed (4P) sample. During aging, the vacancy concentration decreases, which will make the climbing of dislocations more difficult. On the other hand, more Cu atoms will diffuse to dislocations, which has a strong effect on pinning dislocations. It is well known that the dynamic balance between dislocation generation and annihilation determines the work hardening rate. During tensile deformation, the impeded climbing and gliding will reduce the dynamic recovery rate of mobile dislocations. Meanwhile, although the decrease of dislocation density in the aged samples is limited, grains can accommodate more newly formed dislocations. Thus, the work hardening rate can be higher than that of the as-deformed (4P) sample, resulting in the higher UTS and UE. However, after aging at 120 ˚C for 30 min, much more Cu atoms will diffuse to GBs and form precipitates,

which decreases the pinning effect of Cu atoms on dislocations. This will result in faster dynamic recovery during tensile deformation, and lower the amounts of accommodated dislocations and thus the UE. In addition, the value of elongation to failure of aged samples is lower compared with the as-deformed (4P) sample, which can be ascribed to the formation of GB precipitates that can act as crack sources.

5. Conclusions

Natural and artificial aging treatments were conducted on a bimodal structured Al-5Cu alloy prepared by ECAP. The results show that a significant improvement of both ultimate tensile strength and uniform elongation without sacrificing the yield strength could be achieved by an artificial aging at 120 ˚C for 2 min. To reveal the underlying strengthening mechanisms, a systematic study on the evolution of grain size, dislocation density, solid solution level of Cu and the precipitation behavior of precipitates has been conducted. The following conclusions can be drawn:

(1) The as-deformed (4P) Al-5Cu alloy shows a substantially different precipitation behavior and an accelerated precipitation kinetics in comparison to the undeformed counterpart. A large amount of incoherent θ precipitates and occasionally θ' precipitates are formed along HABs while no coherent θ'' or semi-coherent θ' precipitates form in bulk of grains during natural aging and artificial aging at low temperatures. The accelerated precipitation kinetics is due to the segregation of Cu at HABs generated during deformation, as well as the enhanced diffusion of Cu from bulk to GBs by the high vacancy concentration and dislocation density.

(2) After aging at 120 ˚C for 2 min, no change in grain size and GB structure while only very limited reduction of dislocation density within grains larger than 100 nm could be detected. The formation of precipitates along GBs causes a significant reduction of the solid solution level of Cu in the matrix, resulting in decreased solid solution strengthening. However, the 120 ˚C-2 min sample shows about the same YS as that of the as-deformed (4P) alloy.

(3) A quantitative evaluation of different strengthening mechanisms reveals that the total contribution from the GB relaxation and the dislocation source-limited strengthening is less than ~10 MPa, and the GB segregation of Cu atoms provide more than ~25 MPa to the YS. Therefore,

comparted to the GB relaxation and the dislocation source-limited strengthening, the GB segregation of Cu atoms plays a more important role in compensation of the YS reduction due to the reduced dislocation strengthening and solid solution strengthening.

(4) The increased UTS and UE can be attributed to the improved work hardening ability influenced by the reduced vacancy concentration and segregation of Cu on dislocations within grains.

(5) After artificial aging at 120 ˚C for a longer time or at higher temperatures, more grain boundary precipitates are formed along HABs. The formation of coarse globular θ precipitates result in depletion of Cu atoms along GBs, and thus the reduced dislocation strengthening and solid solution strengthening cannot be compensated by the GB segregation and GB relaxation strengthening.

Acknowledgements

The authors would like to acknowledge the financial support from Research Council of Norway, under the FRINATEK project 'BENTMAT' (Project number 222173) and China Scholarship Council. The authors also thank Mr. Pål C. Skaret for his assistance during ECAP experiments and tensile testing. LFC thanks the support from the National Key Research and Development Program of China (2016YFB0700401).

References

[1] R.Z. Valiev, T.G. Langdon, Principles of equal-channel angular pressing as a processing tool for grain refinement, Prog. Mater. Sci. 51 (2006) 881-981.
[2] R.Z. Valiev, R.K. Islamgaliev, I.V. Alexandrov, Bulk nanostructured materials from severe plastic deformation, Prog. Mater. Sci. 45 (2000) 103-189.
[3] H.L. Jia, K. Marthinsen, Y.J. Li, Effect of soft Bi particles on grain refinement during severe plastic deformation, Trans. Nonferrous Met. Soc. China 27 (2017) 971-976.
[4] H.L. Jia, R. Bjørge, K. Marthinsen, R.H. Mathiesen, Y.J. Li, Soft particles assisted grain refinement and strengthening of an Al-Bi-Zn alloy subjected to ECAP, Mater. Sci. Eng. A 703 (2017) 304-313.
[5] C. Xu, Z. Horita, T.G. Langdon, The evolution of homogeneity in processing by high-pressure torsion, Acta Mater. 55 (2007) 203-212.
[6] K. Edalati, D. Akama, A. Nishio, S. Lee, Y. Yonenaga, J.M. Cubero-Sesin, Z. Horita, Influence of dislocation–solute atom interactions and stacking fault energy on grain size of single-phase alloys after severe plastic deformation using high-pressure torsion, Acta Mater. 69 (2014) 68-77.
[7] N.Q. Chinh, P. Szommer, Z. Horita, T.G. Langdon, Experimental Evidence for Grain-Boundary Sliding in Ultrafine-Grained Aluminum Processed by Severe Plastic Deformation, Adv. Mater. 18 (2006) 34-39.
[8] X. Huang, N. Kamikawa, N. Hansen, Strengthening mechanisms in nanostructured aluminum, Mater. Sci. Eng. A 483-484 (2008) 102-104.
[9] X. Huang, Tailoring dislocation structures and mechanical properties of nanostructured metals produced by plastic deformation, Scr. Mater. 60 (2009) 1078-1082.

[10] N. Kamikawa, X. Huang, N. Tsuji, N. Hansen, Strengthening mechanisms in nanostructured high-purity aluminium deformed to high strain and annealed, Acta Mater. 57 (2009) 4198-4208.
[11] X. Huang, N. Hansen, N. Tsuji, Hardening by Annealing and Softening by Deformation in Nanostructured Metals, Science 312 (2006) 249-251.
[12] X. Huang, N. Kamikawa, N. Tsuji, N. Hansen, Nanostructured Aluminum and IF Steel Produced by Rolling-a Comparative Study, ISIJ Int. 48 (2008) 1080-1087.
[13] A.A. Popov, I.Y. Pyshmintsev, S.L. Demakov, A.G. Illarionov, T.C. Lowe, A.V. Sergeyeva, R.Z. Valiev, Structural and mechanical properties of nanocrystalleve titanium processed by severe plastic deformation, Scr. Mater. 37 (1997) 1089-1094.
[14] R.Z. Valiev, F. Chmelik, F. Bordeaux, G. Kapelski, B. Baudelet, The Hall-Petch relation in submicro-grained Al-1.5% Mg alloy, Scr. Metall. Mater. 27 (1992) 855-860.
[15] J. Languillaume, F. Chmelik, G. Kapelski, F. Bordeaux, A.A. Nazarov, G. Canova, C. Esling, R.Z. Valiev, B. Baudelet, Microstructures and hardness of ultrafine-grained Ni_3Al, Acta Metall. Mater. 41 (1993) 2953-2962.
[16] A.J. Detor, C.A. Schuh, Microstructural evolution during the heat treatment of nanocrystalline alloys, J. Mater. Res. 22 (2007) 3233-3248.
[17] J. Hu, Y.N. Shi, X. Sauvage, G. Sha, K. Lu, Grain boundary stability governs hardening and softening in extremely fine nanograined metals, Science 355 (2017) 1292-1296.
[18] D. Jang, M. Atzmon, Grain-boundary relaxation and its effect on plasticity in nanocrystalline Fe, J. Appl. Phys. 99 (2006) 083504.
[19] G.J. Tucker, D.L. McDowell, Non-equilibrium grain boundary structure and inelastic deformation using atomistic simulations, Int. J. Plast. 27 (2011) 841-857.
[20] I.A. Ovid'ko, A.G. Sheinerman, R.Z. Valiev, Dislocation emission from deformation-distorted grain boundaries in ultrafine-grained materials, Scr. Mater. 76 (2014) 45-48.
[21] N.V. Govindaraj, R. Bjørge, B. Holmedal, Characterizing Hardening on Annealing of Cold-Rolled Aluminum AA3103 Strips, Metall. Mater. Trans. A 45 (2014) 1597-1608.
[22] Y.M. Wang, S. Cheng, Q.M. Wei, E. Ma, T.G. Nieh, A. Hamza, Effects of annealing and impurities on tensile properties of electrodeposited nanocrystalline Ni, Scr. Mater. 51 (2004) 1023-1028.
[23] T.J. Rupert, J.R. Trelewicz, C.A. Schuh, Grain boundary relaxation strengthening of nanocrystalline Ni–W alloys, J. Mater. Res. 27 (2012) 1285-1294.
[24] Z. Shan, E.A. Stach, J.M.K. Wiezorek, J.A. Knapp, D.M. Follstaedt, S.X. Mao, Grain Boundary-Mediated Plasticity in Nanocrystalline Nickel, Science 305 (2004) 654-657.
[25] L.H. Wang, J. Teng, P. Liu, A. Hirata, E. Ma, Z. Zhang, M.W. Chen, X.D. Han, Grain rotation mediated by grain boundary dislocations in nanocrystalline platinum, Nat. Commun. 5 (2014) 4402.
[26] T.J. Rupert, D.S. Gianola, Y. Gan, K.J. Hemker, Experimental Observations of Stress-Driven Grain Boundary Migration, Science 326 (2009) 1686-1690.
[27] J. Schiøtz, K.W. Jacobsen, A Maximum in the Strength of Nanocrystalline Copper, Science 301 (2003) 1357-1359.
[28] K. Lu, Stabilizing nanostructures in metals using grain and twin boundary architectures, Nat. Rev. Mater. 1 (2016) 16019.
[29] T. Chookajorn, H.A. Murdoch, C.A. Schuh, Design of Stable Nanocrystalline Alloys, Science 337 (2012) 951-954.
[30] A.J. Detor, C.A. Schuh, Tailoring and patterning the grain size of nanocrystalline alloys, Acta Mater. 55 (2007) 371-379.
[31] A.J. Detor, C.A. Schuh, Grain boundary segregation, chemical ordering and stability of nanocrystalline alloys: Atomistic computer simulations in the Ni–W system, Acta Mater. 55 (2007) 4221-4232.
[32] A.R. Kalidindi, C.A. Schuh, Stability criteria for nanocrystalline alloys, Acta Mater. 132 (2017) 128-137.
[33] J.R. Trelewicz, C.A. Schuh, Grain boundary segregation and thermodynamically stable binary nanocrystalline alloys, Phys. Rev. B 79 (2009) 094112.
[34] H.L. Jia, R. Bjørge, K. Marthinsen, Y.J. Li, The deformation and work hardening behaviour of a SPD processed Al-5Cu alloy, J. Alloys Compd. 697 (2017) 239-248.

[35] H. Zhong, P.A. Rometsch, X.D. Wu, L.F. Cao, Y. Estrin, Influence of pre-ageing on the stretch formability of Al-Mg-Si automotive sheet alloys, Mater. Sci. Eng. A 697 (2017) 79-85.
[36] M. Zha, Y.J. Li, R.H. Mathiesen, R. Bjørge, H.J. Roven, Microstructure evolution and mechanical behavior of a binary Al–7Mg alloy processed by equal-channel angular pressing, Acta Mater. 84 (2015) 42-54.
[37] Y. Huang, J.D. Robson, P.B. Prangnell, The formation of nanograin structures and accelerated room-temperature theta precipitation in a severely deformed Al–4wt.% Cu alloy, Acta Mater. 58 (2010) 1643-1657.
[38] D. Vaughan, Grain boundary precipitation in an Al-Cu alloy, Acta Metall. 16 (1968) 563-577.
[39] P. Cui, T.S. Kê, Anelastic relaxation peak associated with the presence of incoherent θ phase in Al-4wt.%Cu alloy, Mater. Sci. Eng. A 150 (1992) 281-288.
[40] R.K.W. Marceau, G. Sha, R. Ferragut, A. Dupasquier, S.P. Ringer, Solute clustering in Al–Cu–Mg alloys during the early stages of elevated temperature ageing, Acta Mater. 58 (2010) 4923-4939.
[41] M.J. Starink , N. Gao, L. Davin, J. Yan, A. Cerezo, Room temperature precipitation in quenched Al–Cu–Mg alloys: a model for the reaction kinetics and yield strength development, Philos. Mag. 85 (2005) 1395-1417.
[42] N.A. Gjostein, F.N. Rhines, Absolute interfacial energies of [001] tilt and twist grain boundaries in copper, Acta Metall. 7 (1959) 319-330.
[43] H. Mecking, U.F. Kocks, Kinetics of flow and strain-hardening, Acta Metall. 29 (1981) 1865-1875.
[44] A. Matthiessen, C. Vogt, On the influence of temperature on the electric conducting-power of alloys, Philos. Trans. R. Soc. London 154 (1864) 167-200.
[45] T.S. Orlova, A.M. Mavlyutov, A.S. Bondarenko, I.A. Kasatkin, M.Y. Murashkin, R.Z. Valiev, Influence of grain boundary state on electrical resistivity of ultrafine grained aluminium, Philos. Mag. 96 (2016) 2429-2444.
[46] E. Botcharova, J. Freudenberger, L. Schultz, Mechanical and electrical properties of mechanically alloyed nanocrystalline Cu–Nb alloys, Acta Mater. 54 (2006) 3333-3341.
[47] Y. Miyajima, S.-Y. Komatsu, M. Mitsuhara, S. Hata, H. Nakashima, N. Tsuji, Change in electrical resistivity of commercial purity aluminium severely plastic deformed, Philos. Mag. 90 (2010) 4475-4488.
[48] A.S. Karolik, A.A. Luhvich, Calculation of electrical resistivity produced by dislocations and grain boundaries in metals, J. Phys.: Condens. Matter 6 (1994) 873.
[49] S. Komatsu, M. Ikeda, T. Muramatsu, M. Matsuo, Estimation of Solute Fe Concentration in Commercial Pure Aluminium, Key Eng. Mater. 44-45 (1991) 31-56.
[50] S.I. Hong, M.A. Hill, Mechanical stability and electrical conductivity of Cu–Ag filamentary microcomposites, Mater. Sci. Eng. A 264 (1999) 151-158.
[51] N. Takata, S.-H. Lee, N. Tsuji, Ultrafine grained copper alloy sheets having both high strength and high electric conductivity, Mater. Lett. 63 (2009) 1757-1760.
[52] X.M. Luo, Z.M. Song, M.L. Li, Q. Wang, G.P. Zhang, Microstructural Evolution and Service Performance of Cold-drawn Pure Aluminum Conductor Wires, J. Mater. Sci. Technol. 33 (2017) 1039-1043.
[53] W. Lechner, W. Puff, B. Mingler, M.J. Zehetbauer, R. Würschum, Microstructure and vacancy-type defects in high-pressure torsion deformed Al–Cu–Mg–Mn alloy, Scr. Mater. 61 (2009) 383-386.
[54] Y.J. Li, L. Arnberg, Quantitative study on the precipitation behavior of dispersoids in DC-cast AA3003 alloy during heating and homogenization, Acta Mater. 51 (2003) 3415-3428.
[55] S.A. Court, K.P. Hicklin, D.J. Lloyd, The ageing and thermal recovery behaviour of Al-Mg-Cu alloys, Mater. Sci. Forum 396 (2002) 1031-1036.
[56] E. Ma, T.D. Shen, X.L. Wu, Nanostructured metals: Less is more, Nat. Mater. 5 (2006) 515-516.
[57] W. Zeng, Y. Shen, N. Zhang, X. Huang, J. Wang, G. Tang, A. Shan, Rapid hardening induced by electric pulse annealing in nanostructured pure aluminum, Scr. Mater. 66 (2012) 147-150.
[58] A. Hasnaoui, H. Van Swygenhoven, P.M. Derlet, On non-equilibrium grain boundaries and their effect on thermal and mechanical behaviour: a molecular dynamics computer simulation, Acta Mater. 50 (2002) 3927-3939.

[59] R.Z. Valiev, N.A. Enikeev, M.Y. Murashkin, V.U. Kazykhanov, X. Sauvage, On the origin of the extremely high strength of ultrafine-grained Al alloys produced by severe plastic deformation, Scr. Mater. 63 (2010) 949-952.
[60] J.P. Hirth, J. Lothe, Theory of dislocations, McGraw-Hill, New York; London, 1968.
[61] D.D. Zhao, O.M. Løvvik, K. Marthinsen, Y.J. Li, Segregation of Mg, Cu and their effects on the strength of Al Σ5 (210)[001] symmetrical tilt grain boundary, Acta Mater. 145 (2018) 235-246.
[62] E. Nes, B. Holmedal, E. Evangelista, K. Marthinsen, Modelling grain boundary strengthening in ultra-fine grained aluminum alloys, Mater. Sci. Eng. A 410 (2005) 178-182.
[63] N.Q. Vo, J. Schäfer, R.S. Averback, K. Albe, Y. Ashkenazy, P. Bellon, Reaching theoretical strengths in nanocrystalline Cu by grain boundary doping, Scr. Mater. 65 (2011) 660-663.

Table 1. Tensile properties of the as-deformed (4P) and artificially aged 4P Al-5 wt.% Cu samples.

Condition	EC (MS/m)	YS (MPa)	UTS (MPa)	UE (%)	EF (%)
4P	20.5	473.3	506.7	5.1	27.0
4P+120 ℃-2 min	21.6	471.7	520.5	6.0	25.5
4P+120 ℃-5 min	22.0	451.4	501.4	6.4	24.2
4P+120 ℃-15 min	22.5	420.7	482.6	8.7	23.1
4P+120 ℃-30 min	22.7	390.3	454.5	6.4	22.4
4P+150 ℃-5 min	23.6	384.4	441.4	6.9	22.1
4P+150 ℃-15 min	24.3	370.0	430.0	6.4	22.0
4P+150 ℃-30 min	24.7	372.5	425.0	5.2	22.0

Table 2. Geometrically necessary dislocation (GND) density of the as-deformed (4P) and artificially aged 4P Al-5 wt.% Cu samples.

Condition	Coarse micron-sized grain (> 2 μm)	Fine micron-sized grain (1-2 μm)	Submicron-sized grain (100 nm-1 μm)
4P	~2.2×10^{14} m^{-2}	~1.8×10^{14} m^{-2}	~1.3×10^{15} m^{-2}
4P+120 ℃-2 min	~2.0×10^{14} m^{-2}	~1.5×10^{14} m^{-2}	~1.2×10^{15} m^{-2}
4P+120 ℃-30 min	~1.8×10^{14} m^{-2}	~1.3×10^{14} m^{-2}	~8.0×10^{14} m^{-2}

Table 3. Decreased dislocation strengthening and solid solution strengthening in the as-deformed (4P) samples after aging at 120 ˚C for 2 min and 30 min, respectively.

Condition	Decreased yield strength ($\Delta\sigma_y$)	Decreased dislocation strengthening ($\Delta\sigma_D$)			Decreased solid solution strengthening ($\Delta\sigma_{SS}$)
		Coarse micron-sized grain (> 2 μm)	Fine micron-sized grain (1-2 μm)	Submicron-sized grain (100 nm-1 μm)	
4P+120 ℃-2 min	~2 MPa	~5 MPa	~8 MPa	~10 MPa	~26 MPa
4P+120 ℃-30 min	~83 MPa	~10 MPa	~14 MPa	~54 MPa	~49 MPa

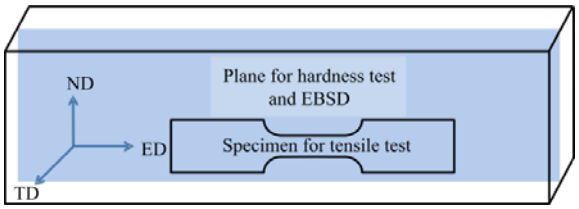

Fig. 1. Sketch of the sample for ECAP. ND, TD and ED are abbreviations of the normal, transverse and extrusion directions, respectively. The regions for EBSD observations, hardness and tensile tests are also indicated.

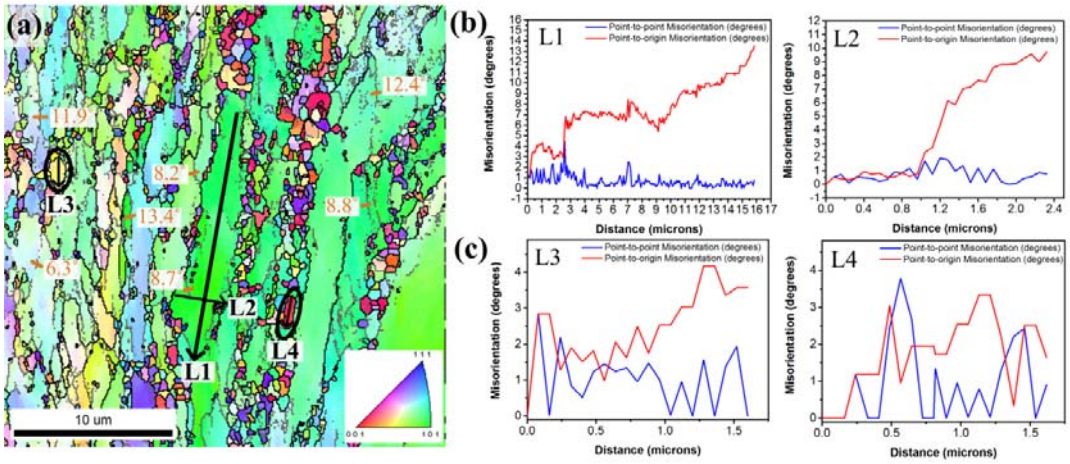

Fig. 2. (a) EBSD orientation map of the as-deformed (4P) sample, (b) and (c) misorientation profiles measured along lines L1-L4, as shown in (a). Grey and black lines in (a) depict boundaries with misorientation angles of $5^\circ \leq \theta < 15^\circ$ and $\theta \geq 15^\circ$, respectively. In (a), some misorientation angles of LABs are labelled.

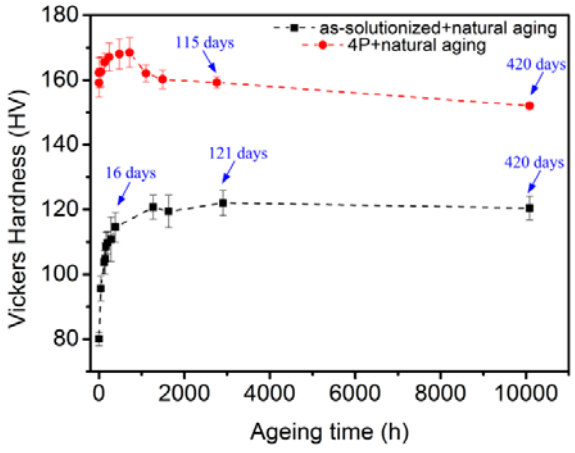

Fig. 3. Evolution of Vickers hardness during natural aging for the as-solutionized and as-deformed (4P) Al-5Cu samples, respectively.

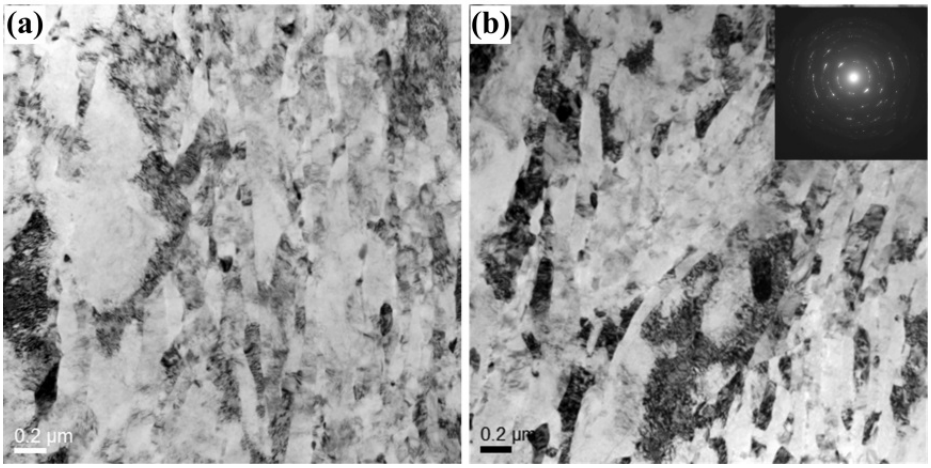

Fig. 4. TEM images of (a) the as-deformed (4P) sample and (b) the as-deformed (4P) sample after one-month natural aging. The inset in (b) is the representative diffraction pattern.

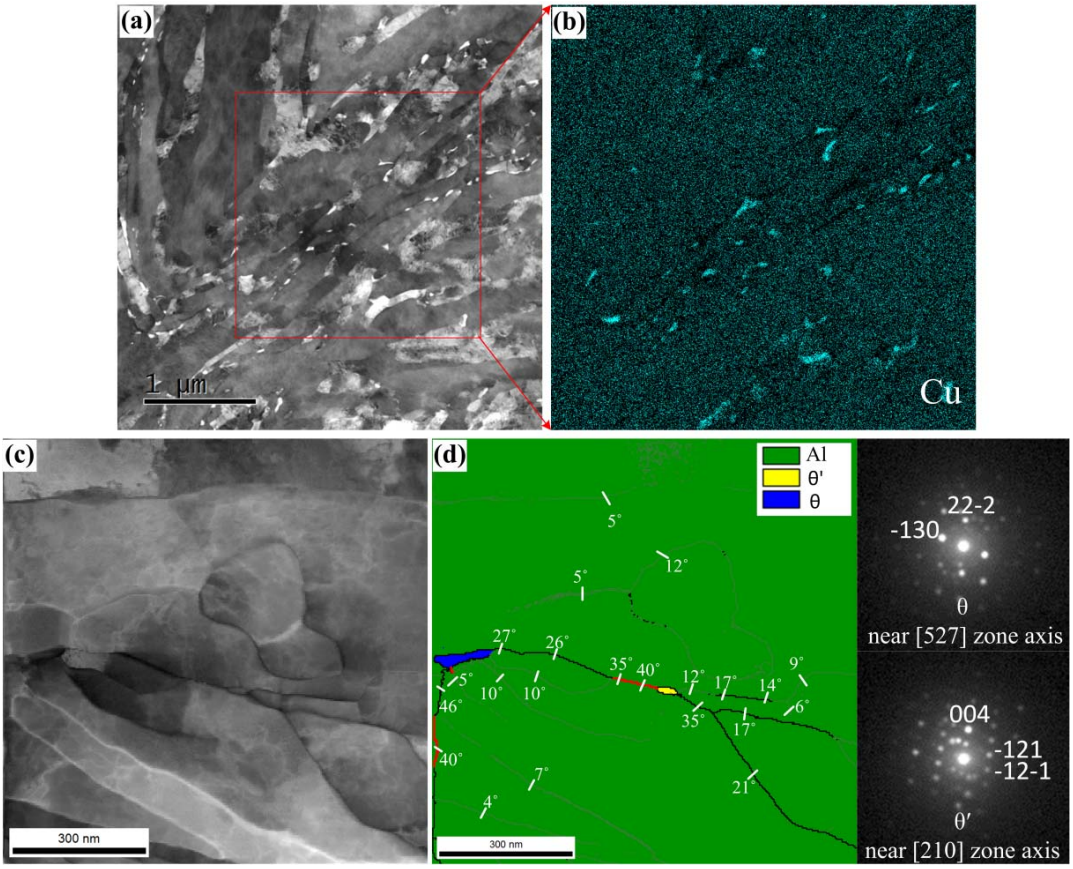

Fig. 5. Microstructure of the as-deformed (4P) sample after one-month natural aging. (a) HAADF-STEM image, (b) EDS map of the Cu element for the framed area in (a), (c) SPED image quality map, and (d) phase map with corresponding diffraction patterns for the θ and θ' precipitates, respectively. The red, light grey and coarse black lines depict Σ9 boundaries, and general boundaries with misorientation angles of $2^\circ \leq \theta < 15^\circ$ and $\theta \geq 15^\circ$, respectively.

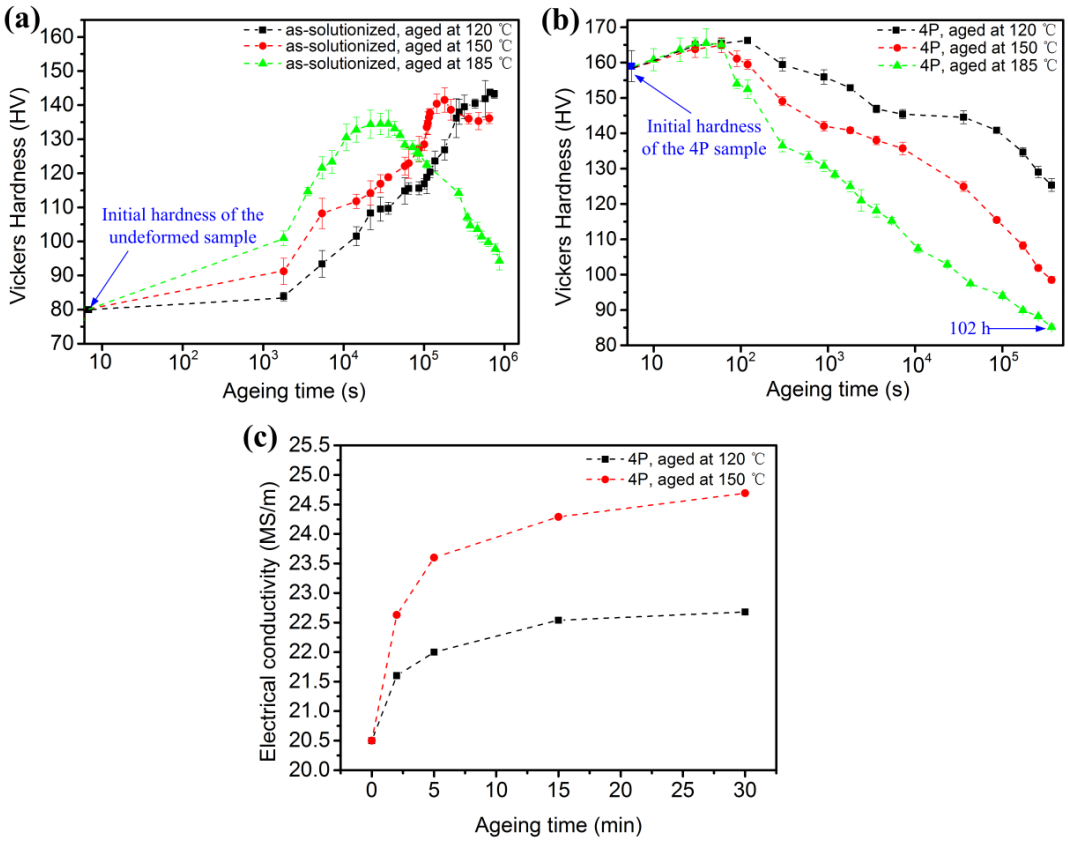

Fig. 6. (a) Evolution of Vickers hardness for the as-solutionized Al-5Cu alloy; (b) and (c) evolution of Vickers hardness and electrical conductivity for the as-deformed (4P) Al-5Cu alloy during artificial aging, respectively. Artificial aging temperatures are 120 ˚C, 150 ˚C and 185 ˚C, respectively.

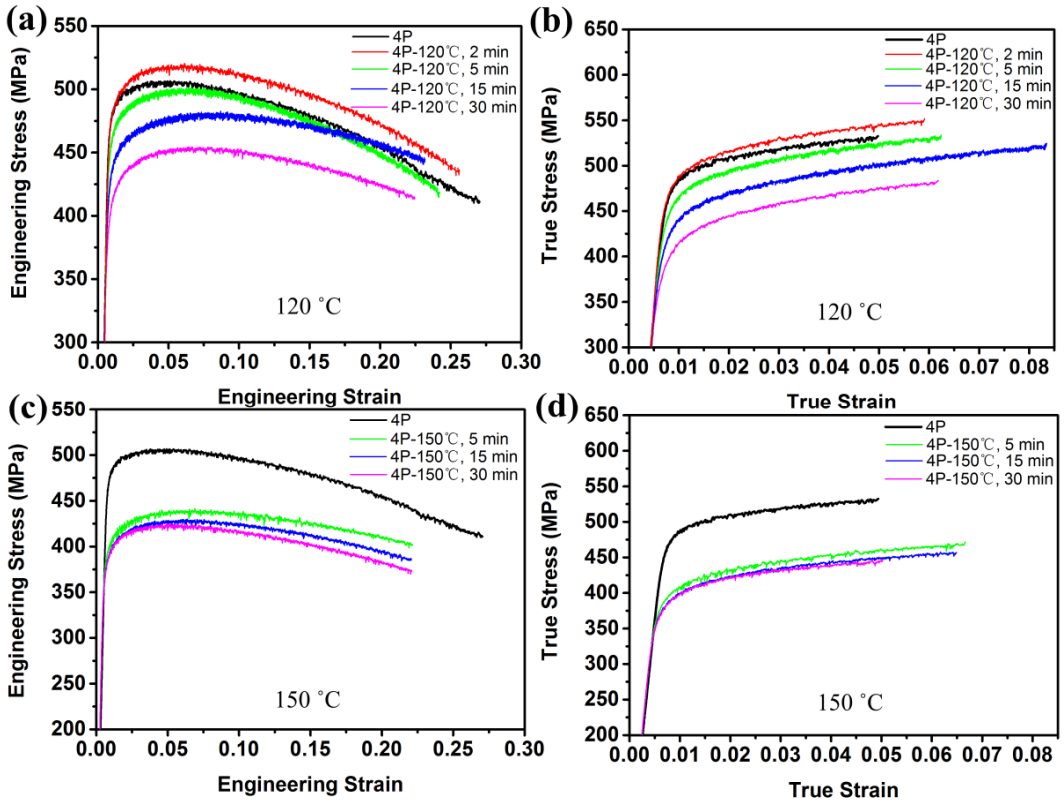

Fig. 7. (a) Engineering tensile stress-strain curves and (b) true stress-strain curves of the as-deformed (4P) samples aged at 120 ˚C, (c) engineering tensile stress-strain curves and (d) true stress-strain curves of the as-deformed (4P) samples aged 150 ˚C. For comparison, the plots for the as-deformed (4P) sample are also included.

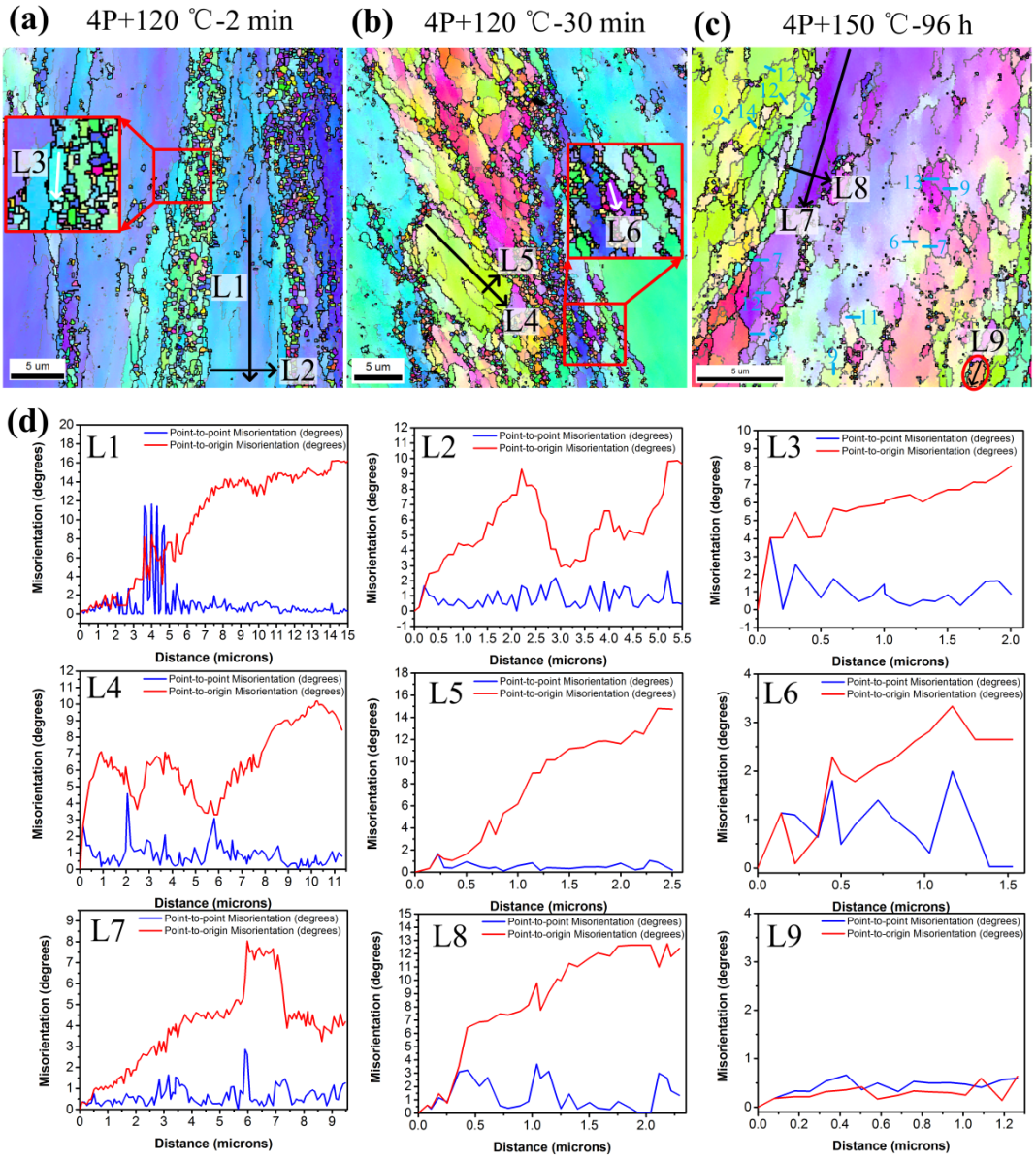

Fig. 8. EBSD maps of the aged samples, (a) 4P+120 ˚C-2 min, (b) 4P+120 ˚C-30 min, (c) 4P+150 ˚C-96 h. (d) Misorientation profiles measured along the lines L1-L9 shown in Fig. (a)-(c). Narrow grey and coarse black lines in (a)-(c) depict boundaries with misorientation angles of $5^\circ \leq \theta < 15^\circ$ and $\theta \geq 15^\circ$, respectively.

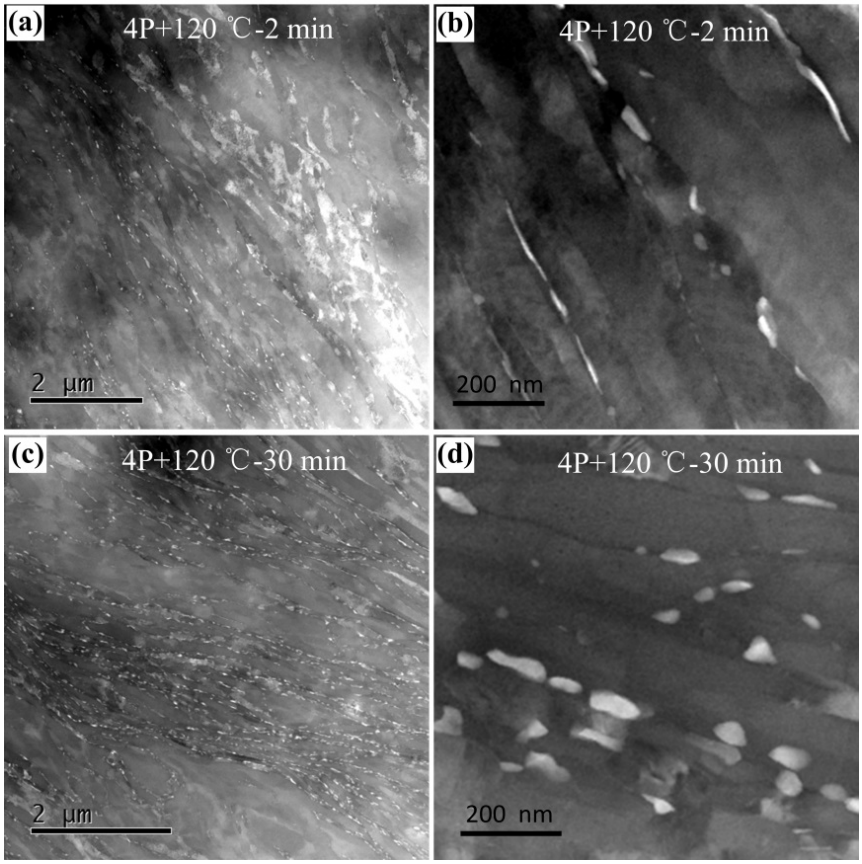

Fig. 9. (a) and (b) HAADF-STEM images of the 4P+120 ˚C-2 min sample; (c)-(d) HAADF-STEM images of the 4P+120 ˚C-30 min sample.

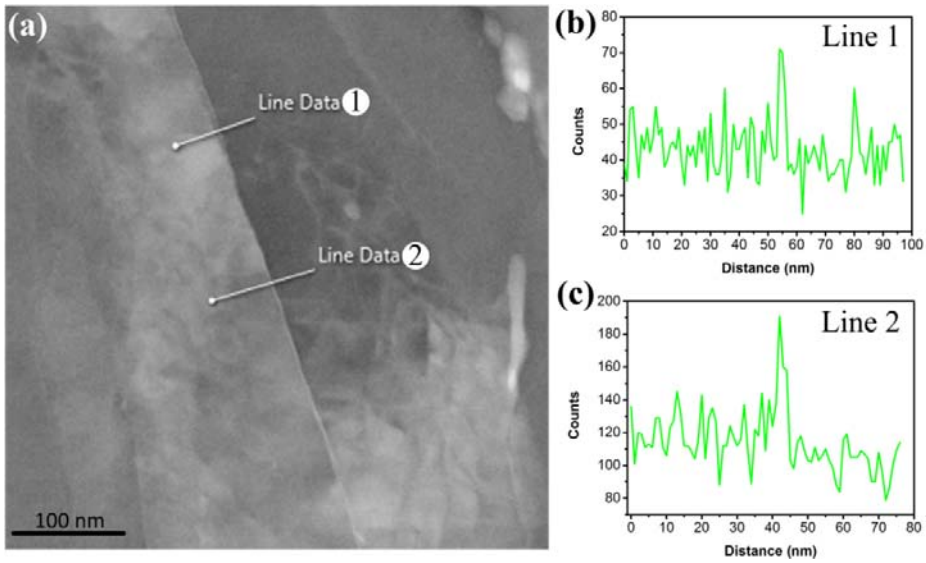

Fig. 10. Segregation of Cu atoms at grain boundaries in the 4P+120 ˚C-2 min sample. (a) STEM image showing two lines across a grain boundary, and (b) and (c) EDS line scan curves showing distribution of Cu along Line 1 and Line 2 labelled in (a).

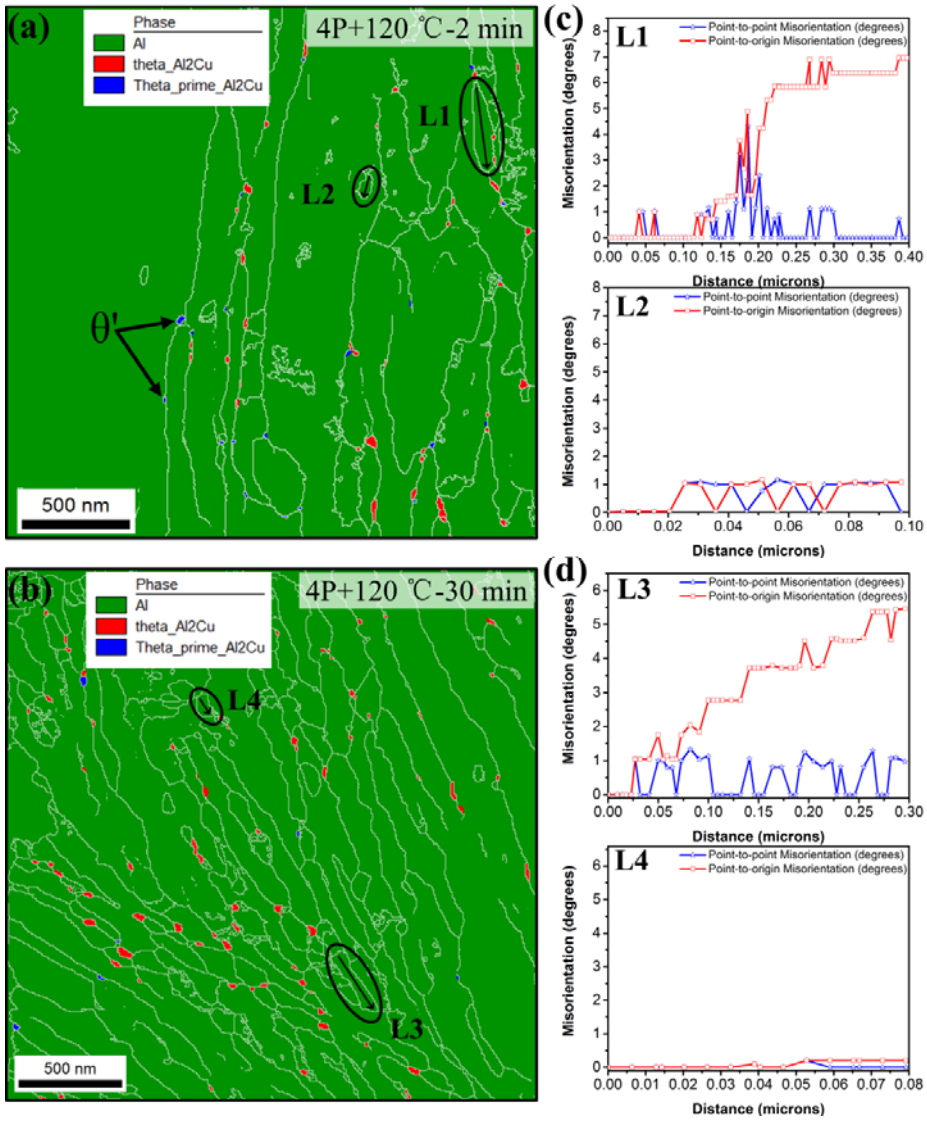

Fig. 11. TEM-SPED phase maps of (a) 4P+120 ℃-2 min sample, and (b) 4P+120 ℃-30 min sample; (c) and (d) show misorientation profiles along the lines L1-L4 encircled by the black ovals in (a) and (b). In (a)-(b), white lines depict boundaries with misorientation angles of $\theta \geq 15^{\circ}$ and the inset is the color code for different phases.

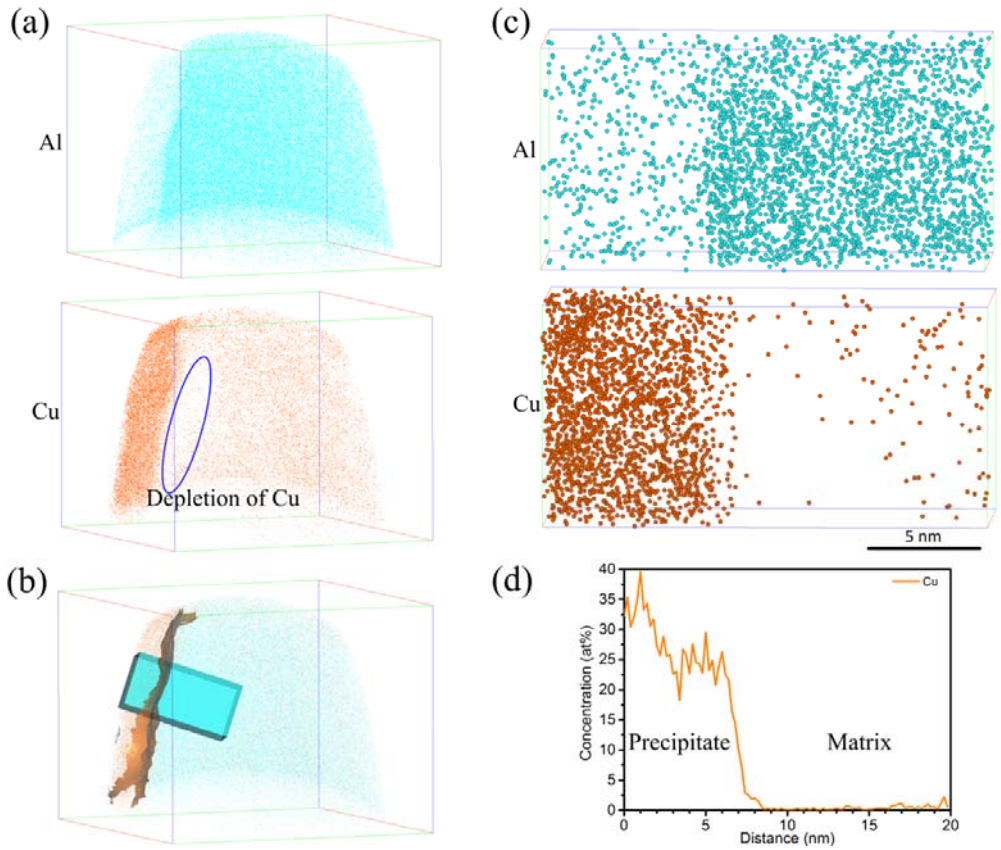

Fig. 12. APT characterizations of the as-deformed (4P) Al-5Cu sample aged at 120 ˚C for 2 min. (a) 3D atom maps of an analyzed volume (52nm × 52nm × 42nm); (b) 3D morphology of the grain or phase boundary; (c) 3D atom distributions in the highlighted volume (10nm × 10nm × 20nm) in (c); (d) 1D concentration profile of Cu across the phase interface.

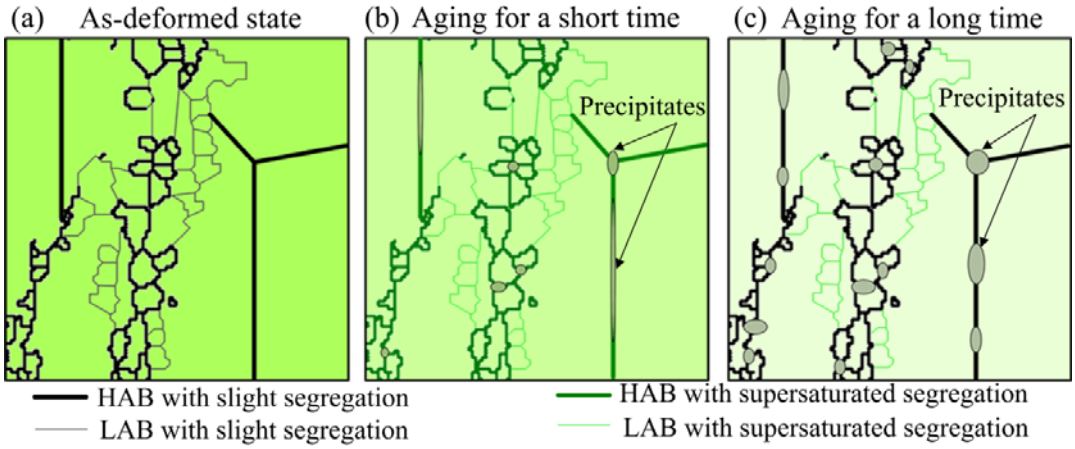

Fig. 13. Schematic for segregation of Cu atoms, and formation of precipitates along HABs during aging treatment. The different colors of the matrix indicate different solid solution level of Cu in the matrix.

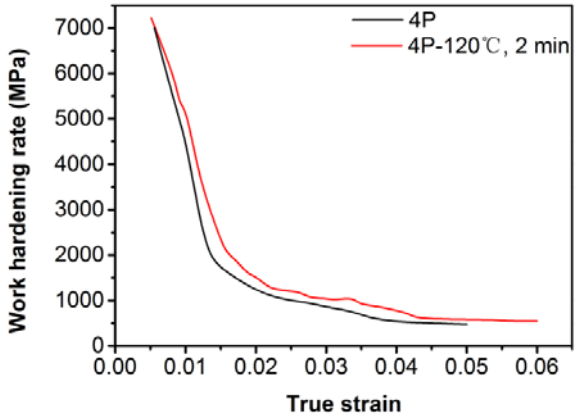

Fig. 14. Work hardening rate curves of the as-deformed (4P) and 4P+120 ˚C-2 min samples.